



## OPEN ACCESS

## EDITED BY

Zhengmao Li,  
Aalto University, Finland

## REVIEWED BY

Minglei Bao,  
Zhejiang University, China  
Jianhui Meng,  
North China Electric Power University,  
China

## \*CORRESPONDENCE

Jie Chen,  
✉ chenjie@cma.gov.com

RECEIVED 23 July 2023

ACCEPTED 24 August 2023

PUBLISHED 12 September 2023

## CITATION

Li J, Chen J, Yu H, Jiang M, Lu Z, Zhou Y, Wang S and Fan J (2023), Wildfire monitoring technologies of transmission line corridors based on Fengyun-3E satellite imaging. *Front. Energy Res.* 11:1265516. doi: 10.3389/fenrg.2023.1265516

## COPYRIGHT

© 2023 Li, Chen, Yu, Jiang, Lu, Zhou, Wang and Fan. This is an open-access article distributed under the terms of the [Creative Commons Attribution License \(CC BY\)](https://creativecommons.org/licenses/by/4.0/). The use, distribution or reproduction in other forums is permitted, provided the original author(s) and the copyright owner(s) are credited and that the original publication in this journal is cited, in accordance with accepted academic practice. No use, distribution or reproduction is permitted which does not comply with these terms.

# Wildfire monitoring technologies of transmission line corridors based on Fengyun-3E satellite imaging

Jinsong Li<sup>1</sup>, Jie Chen<sup>2\*</sup>, Hua Yu<sup>1</sup>, Min Jiang<sup>1</sup>, Zhumao Lu<sup>1</sup>, You Zhou<sup>3</sup>, Shuai Wang<sup>1</sup> and Jingjing Fan<sup>1</sup>

<sup>1</sup>State Grid Shanxi Electric Power Research Institute, Taiyuan, China, <sup>2</sup>National Satellite Meteorological Center, Beijing, China, <sup>3</sup>State Key Laboratory of Disaster Prevention and Reduction for Power Grid, Changsha University of Science and Technology, Changsha, China

Facing towards the Carbon Neutrality goal by 2060, renewable energy sources are boosted in China in the past decade. Either these renewables or power systems are sensitive and vulnerable to natural disasters, such as wildfire and typhoon. In this paper, a fire spot identification algorithm is proposed for wildfire disaster occurred in transmission line corridors based on Fengyun-3E (FY-3E). It mitigates the effect of large observation of solar zenith angle, as well as changes of satellite views, on the infrared channel detection. And cloud information under complex atmospheric conditions is analyzed to extract the cloud pixel fire spot, which decreases false ratio of fire-spot alerts. According to the analysis of hybrid pixel linear spectrums, the fire-spot detection sensitivity of FY-3E is four times as that of geostationary meteorological satellites. The effectiveness of the proposed algorithm was confirmed by an application in the Shanxi province power grid of State Grid in China. It shows that and the FY-3E has a superiority in wildfire monitoring for power system in terms of fire detection sensitivity, spatial range accuracy, and positioning accuracy. Compared to geostationary meteorological satellites, the fire locating accuracy of FY-3E is increased by more than one-fold. This research can assist the operation and maintenance departments of transmission lines to rapidly detect wildfire, thereby reducing the damage of wildfires on the power grid.

## KEYWORDS

Fengyun-3E, transmission lines fires, fire spot identification, dawn-dusk monitoring, satellite remote sensing

## 1 Introduction

Reducing carbon missions and achieving “Carbon Neutrality” requires the developing and utilizing of renewables such as wind power and solar energy on a large scale. In China, the renewable energies are generally oriented in Northwest and offshore regions, the transmission of them requires long-distance transmission lines in areas with dense vegetation, such as forests and grasslands (Anagnostatos et al., 2011; Wang, 2022). In this case, wildfires caused by lightning or industrial and agricultural activities reduce the insulation of overhead transmission line greatly, which induces tripping failures to affect the reliability of power system (Fonseca et al., 1990; El-Zohri et al., 2013; You et al., 2013; Wang et al., 2016). It is necessary to monitor wildfires in transmission corridors and mitigate the threats of wildfire to transmission line operations timely and accurately.

TABLE 1 Basic performance of meteorological satellites.

	Type	Time of passing territory	Spatial resolution (km)
NOAA18	PMS	11:28, 22:52	1.0
NOAA19	PMS	09:20, 20:45	1.0
NPP	PMS	01:30, 13:30	0.375/0.75
NOAA20	PMS	01:30, 13:30	0.375/0.75
FY-3C	PMS	10:15, 22:15	1.0
FY-3D	PMS	02:00, 14:00	1.0
FY-3E	PMS	05:30, 17:30	1.0
H8	GMS	All day	2.0
GK-2A	GMS	All day	2.0

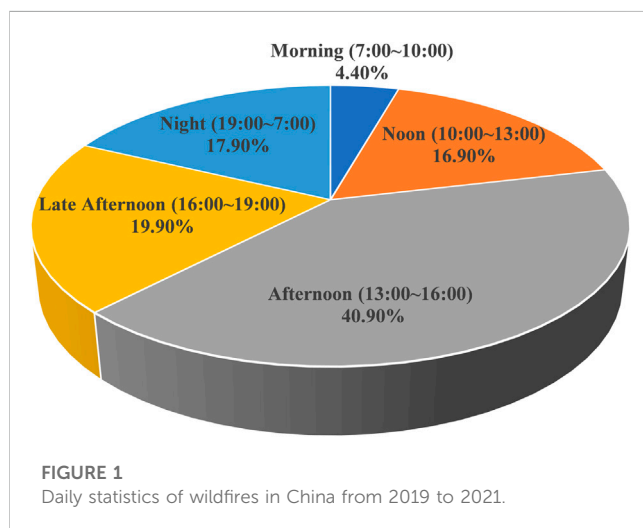


FIGURE 1  
Daily statistics of wildfires in China from 2019 to 2021.

Currently, wildfires in transmission corridors are the primarily monitored by manned patrols, aircraft cruise, visible and infrared image devices, and meteorological satellites (Su et al., 2019). As a vital tool, meteorological satellites offers an inexpensive monitoring capacity of wide area with a high observation frequency (Liang et al., 2020; Zhou et al., 2020). The meteorological satellites can be divided into two types based on their orbits: Polar-orbiting Meteorological Satellites (PMSs) and Geosynchronous Meteorological Satellites (GMSs). The National Oceanic and Atmospheric Administration (NOAA), National Polar-orbiting Operational Environmental Satellite System Preparatory Project (NPP), and Fengyun-3 series (FY-3C, FY-3D) are the commonly used polar-orbiting meteorological satellites. Himawari-8 (H8) and Geo-Kompsat-2A (GK-2A) are examples of geostationary meteorological satellites (Frost and Annegarn, 2007; Blackett, 2015; Zhang et al., 2017; Lu et al., 2018; Chen et al., 2019; Su et al., 2019). The basic performance of these meteorological satellites is compared in Table 1.

Although the GMSs have an extremely high temporal resolution, there are still lots of missing small fires in

transmission line corridors due to the weaker spatial resolution and limited detecting sensitivity. PMSs provide a global wildfire observation by scanning the Earth twice daily with a constant local solar time (Chen et al., 2022b). Besides, the distance between PMSs and Earth are only one-fifth as that of GMSs, causing a higher spatial resolution of PMSs. Artificial fire tests show that the smallest fire area that EOS/MODIS and FY-3D/MERSI-II can identify is approximately 100 m<sup>2</sup> (Giglio, 2010; Zheng et al., 2020). However, the transit durations of the PMSs are primarily concentrated in the hours of 9:00–11:00 and 13:00–16:00 in China (Hillger et al., 2013; Yu and Wu, 2016), whereas wildfires often happen at the dusk hours (16:00–19:00), as shown in Figure 1 that the frequency of wildfire during transit is second only to the afternoon hours in China. The lack of transit monitoring by PMSs might results in missed alerts of wildfires.

Fengyun-3E (FY-3E) has been in operation since March 2022. It is the first operational meteorological satellite to pass over the territory of China during the dawn-dusk hours. Compared to the previous Fengyun series, the detection performance of FY-3E is significantly enhanced by the installation of Medium Resolution Spectral Imager-LL (MERSI-LL) on FY-3E, providing a novel way for monitoring wildfire occurrence at dusk. The National Satellite Meteorological Centre has conducted extensive research on wildfire identification algorithms based on the satellite data of Fengyun-3 series (Shengli and Cheng, 2010; Shan et al., 2021; Chen et al., 2022a). However, differences in spectrometer and monitoring time prevented traditional wildfire identification algorithms from being applied to the FY-3E.

This work proposes a wildfire identification algorithm of the FY-3E/MERSI-LL considering infrared radiation corrections and complex atmospheric conditions of dawn-dusk hours. The impacts of mid-infrared channels of the FY-3E/MERSI-LL, H8/AHI, and GK-2A/AMI on the identification sensitivity of fire spot are compared by using a hybrid pixel linear decomposition method. FY-3E was applied for the monitoring and early warning of wildfires in transmission line corridors for the first time. Engineering practice confirms the effectiveness of the proposed algorithm. And the superiority of FY-3E over H8 and GK-2A PMSs is also compared by engineering application.

TABLE 2 Major parameters of MERSI-LL bands of FY-3E.

	Central wavelength (μm)	Bandwidth (nm)	Spatial resolution (km)	Main uses
1	0.7	400	1	Low-light sensing in night
2	3.8	180	1	Fire, temperature of land surface and sea surface, cloud
3	4.05	155	1	Fire
4	7.2	500	1	Atmosphere, water vapour
5	8.55	300	1	Rolling clouds, cloud
6	10.8	1,000	0.25	Temperature of land surface and sea surface, cloud
7	12	1,000	0.25	Temperature of land surface and sea surface, cloud

## 2 Method for monitoring wildfires on FY-3E

FY-3E is the first operational dawn–dusk orbit PMS independently created by China. It was launched at 7:28 p.m. on 5 July 2021 from the Jiuquan Satellite Launch Centre and put into service in March 2022. The launch weight of FY-3E is 2.3t. And its design life is 8 years. The satellite’s orbit has an inclination of 98.75° and a nominal altitude of approximately 836 km. It passes over the ground in China twice a day at 5:30 a.m. and 5:30 p.m. Beijing time. FY-3E is equipped with the newly developed MERSI-LL with seven observation bands which includes a Day Night Band and six thermal infrared bands. The primary technical specifications of MERSI-LL bands are listed in Table 2 (Dong et al., 2022; Xie et al., 2022; Zhang et al., 2022). Two of the infrared split-window bands have a spatial resolution of 250 m, and the remaining bands are of 1000 m resolution. Compared to the H8 and GK-2A GMSs, which are being used extensively for wildfire monitoring in China, FY-3E has an enhanced resolution of the thermal infrared bands.

### 2.1 Wildfire monitoring principle for FY-3E/MERSI-LL

Based on Wien’s displacement law, the black-body radiation curves for peak at different wavelengths that are inversely proportional to the temperatures. The surface radiation at room temperature (approximately 290 K) has a peak wavelength in the 11-μm. And the temperature of forest and grassland wildfire is generally higher than 750 K, the peak wavelength of its spectral radiance is shifted in the short-wave direction closing to the 4-μm mid-infrared band. Therefore, it can detect wildfire in time by comparing the difference between the burning and non-burning radiations in 11-μm and 4-μm bands (Martín et al., 1999; Roy et al., 2013; Wooster et al., 2021; Fan et al., 2022).

The FY-3E/MERSI-LL has a 3.8-μm mid-infrared band with a resolution of 1 km, and 10.8-μm and 12-μm far-infrared bands with resolutions of 250 m. Even with a higher resolution, a pixel of the far infrared bands covers an area with approximately 62,500 m<sup>2</sup>, which is larger than general forest and grassland fires. Therefore, a pixel covering a wildfire can be considered as a hybrid pixel. According to the linear decomposition method

for hybrid pixel, the radiant energy of a hybrid pixel is a linear combination of the radiant energy of the objects. That is, the weighted average of the radiant energy of each object as a proportion of the area.

$$L_t = \left( \sum_{i=1}^n \Delta S_i L_{Ti} \right) / S \tag{1}$$

where  $L_t$  is the radiant energy of the hybrid pixel;  $t$  is the equivalent blackbody temperature corresponding to the irradiance;  $\Delta S_i$  is the area of the  $i$ th subregion in the pixel;  $L_{Ti}$  is the radiant energy of the  $i$ th subregion (in  $W \cdot m^{-2} \cdot sr^{-1} \cdot \mu m^{-1}$ );  $T_i$  is the temperature of the  $i$ th subregion; and  $S$  is the total area of the pixel.

When a wildfire occurred in a region, the temperature and radiant energy of the wildfire region are several hundred times greater than those of other regions. The radiant energy of an pixel containing the wildfire spot can be analyzed by following equation (Dozier, 1981):

$$L_{mix} = P \cdot L_{ft} + (1 - P) \cdot L_{bg} \\ = P \cdot \frac{C_1 \lambda_i^{-5}}{\pi \left( e^{C_2 / \lambda_i T_{ft}} - 1 \right)} + (1 - P) \cdot \frac{C_1 \lambda_i^{-5}}{\pi \left( e^{C_2 / \lambda_i T_{bg}} - 1 \right)} \tag{2}$$

where  $L_{mix}$  is the radiant energy of the  $i$ th bands for the fire spot pixel;  $P$  represents the ratio of the wildfire area to the whole pixel area;  $L_{ft}$  and  $L_{bg}$  are the radiant energies of the wildfire and the non-fire areas (the background around the wildfire), respectively;  $T_{ft}$  and  $T_{bg}$  are the temperatures of the wildfire pixel and background, respectively;  $\lambda_i$  is the central wavelength of the  $i$ th band for the wildfire pixel;  $C_1 = 1.91043 \times 10^8 W \mu m^4 m^{-2} sr^{-1}$ , and  $C_2 = 1.438768 \times 10^4 \mu m K$ .

The primary criterion for identifying a wildfire is based on whether the brightness temperature of the detected pixel is significantly greater than that of the surrounding pixels. The difference in brightness temperature between the hybrid pixel of the  $i$ th band  $\Delta T_i$ , can be expressed as

$$\Delta T_i = T_{mix} - T_{bg} = \frac{C_2}{\lambda_i Ln \left( 1 + \frac{C_1}{\pi \lambda_i^5 L_{mix}} \right)} - \frac{C_2}{\lambda_i Ln \left( 1 + \frac{C_1}{\pi \lambda_i^5 L_{bg}} \right)} \tag{3}$$

where  $T_{mix}$  is the brightness temperature of the hybrid pixel, and  $T_{bg}$  is the brightness temperature of the background pixels,

Assuming a background temperature of 290 K, a wildfire temperature of 800 K, and the fire area is converted into the wildfire proportion of the pixel, the relationship between the brightness temperature increment of the hybrid pixel in the

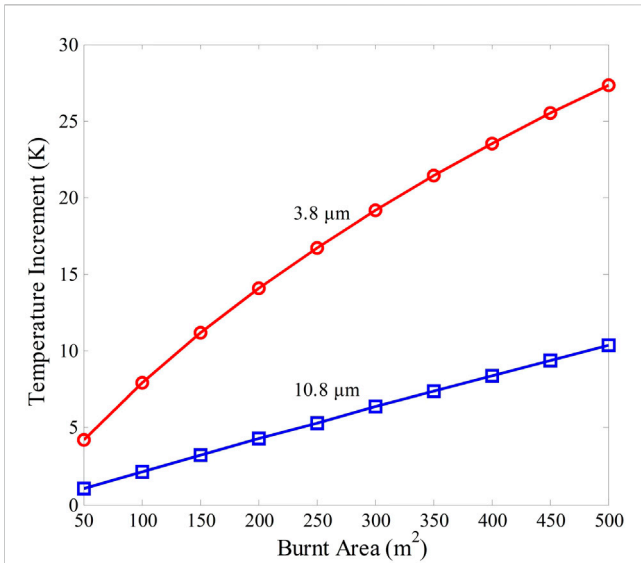


**FIGURE 2**  
Brightness temperature increment of the hybrid pixel for the 3.8- $\mu\text{m}$  and 10.8- $\mu\text{m}$  bands with different fire areas.

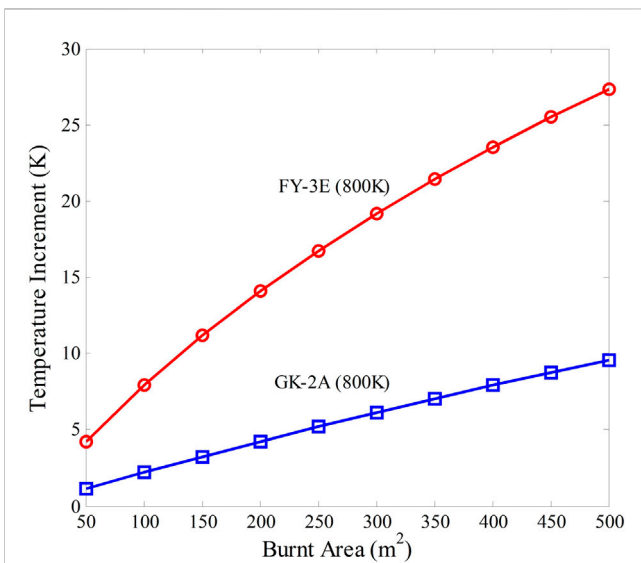


**FIGURE 3**  
Brightness temperature increment for of FY-3E and H8 and GK-2A in the mid-infrared bands.

3.8- $\mu\text{m}$  and 10.8- $\mu\text{m}$  thermal infrared bands and the area of wildfire region is plotted in Figure 2. The brightness temperature increment of the 3.8- $\mu\text{m}$  and 10.8- $\mu\text{m}$  bands steadily increase as the area of wildfire region. And the difference between two bands also increase. Even a small area of wildfire could increase the brightness temperature of mid-infrared channel considerably. Owing to the high sensitivity of brightness temperature for the mid-infrared band to the wildfire, the brightness temperature differences between the wildfire pixel and the surrounding background pixels in the 3.8- $\mu\text{m}$  channel and 10.8- $\mu\text{m}$  bands can be used to identify the wildfire on the surface of Earth.

## 2.2 Sensitive comparison of the mid-infrared bands of FY-3E with H8 and GK-2A

The wildfire detection sensitivity of FY-3E with the GMSs H8 and GK-2A was compared by using Eq 3, as shown in Figure 3. It should be notice that the resolution of 3.8- $\mu\text{m}$  mid-infrared band of FY-3E is 1 km whereas those of H8 and GK-2A are 2 km. When the area of wildfire is 80 m<sup>2</sup>, the area ratio of the wildfire is 0.008% of the whole pixel of the FY-3E whose resolution of the mid-infrared band is 1-km. In this situation, the mid-infrared channel of FY-3E has a brightness temperature increment of approximately 7 K, which exceeds the general identification threshold (6 K). However, brightness temperature increment of the H8 and GK-2A is only 1.8 K. It does not reach the identification threshold until the wildfire area increase to 300 m<sup>2</sup>. The sensitivity of mid-infrared band of the FY-3E is approximately four times as that of the H8 and GK-2A.

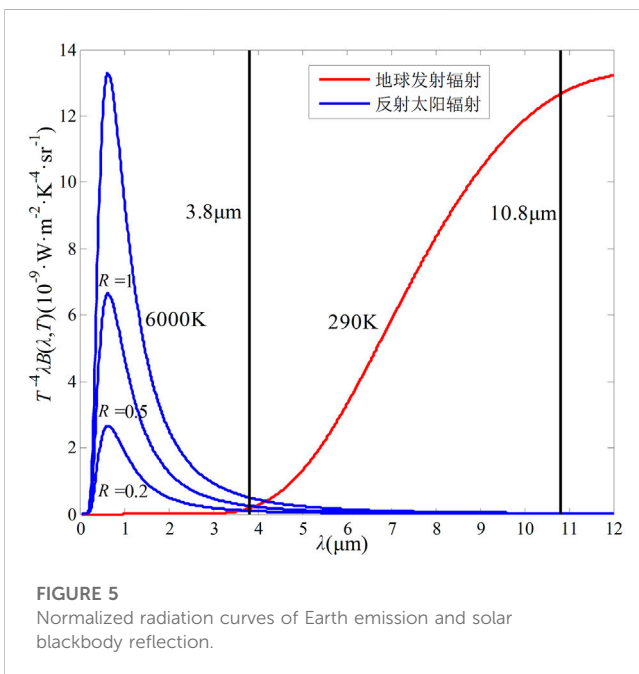
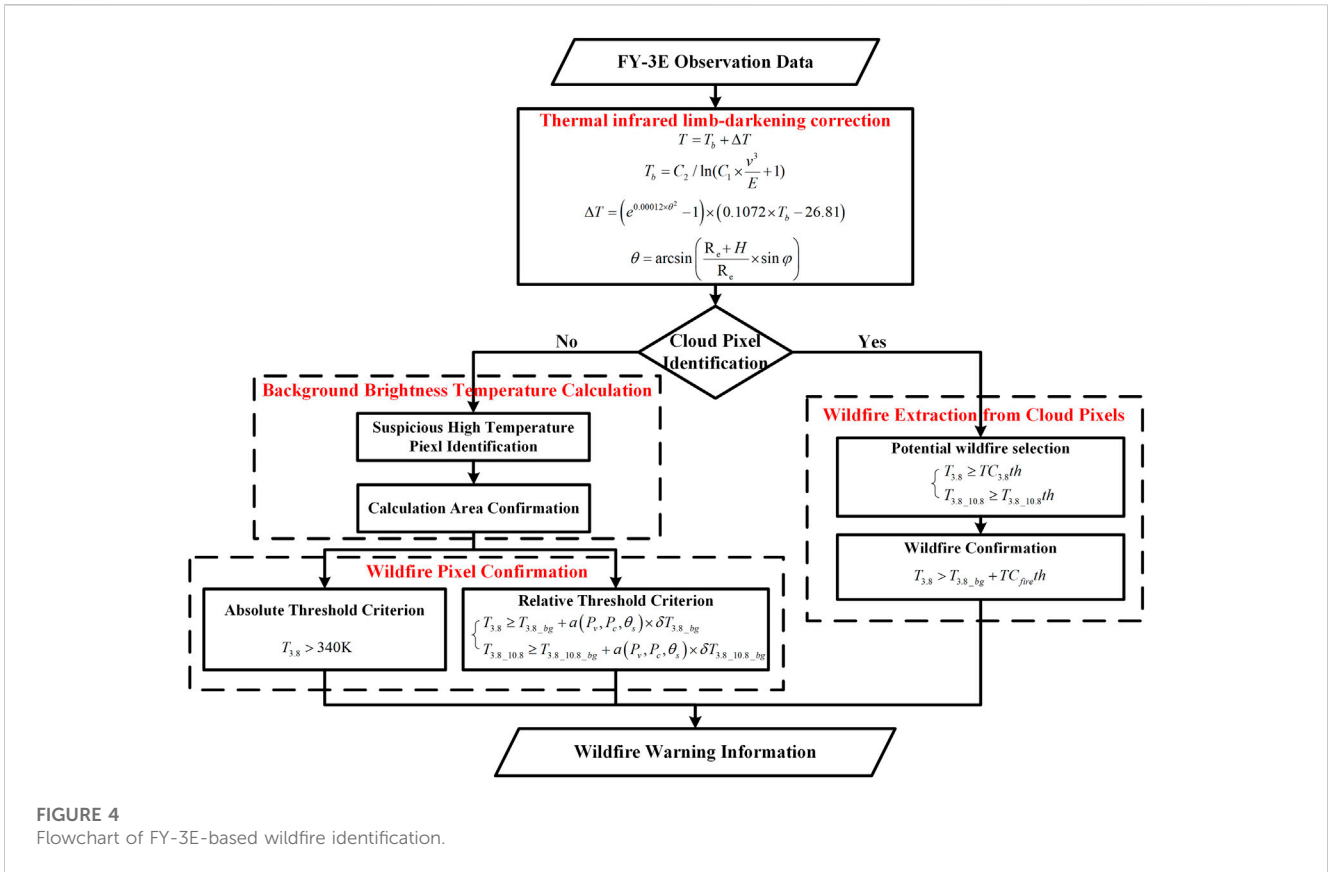
## 3 Wildfire identification algorithm of FY-3E/MERSI-LL

In this study, based on the wildfire identification principles of EOS/MODIS and FY-3D/MERSI-II (Chen et al., 2022a), an wildfire identification algorithm is proposed for FY-3E. The algorithm comprehensively considers the atmospheric conditions during dawn–dusk hours and the instrument characteristics of FY-3E/MERSI-LL. The influence of large solar zenith angle observation conditions and satellite viewing angles on infrared channel detection data is corrected. And the cloud information as well as the wildfire spot under complex atmospheric conditions are extracted. The flowchart of wildfire identification algorithm of FY-3E is shown as Figure 4.

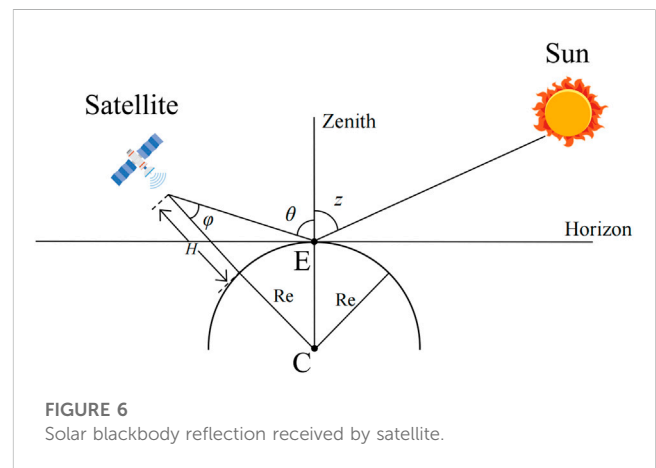
### 3.1 Solar zenith angle correction

Precise acquisition of brightness temperature data in the mid-infrared and far-infrared bands is essential for wildfire identification. Figure 5 shows the normalized radiation curves of Earth emission and solar blackbody reflection. In the figure,  $\lambda$  represents the wavelength of radiation,  $T$  is the absolute temperature,  $B(\lambda, T)$  is the Planck function for  $\lambda$  and  $T$ , and  $R$  is the reflectance. The frequency range of 3.8- $\mu\text{m}$  mid-infrared band is close to the intersection of the Earth emission and solar blackbody reflection curves, whereas the frequency range of 10.8- $\mu\text{m}$  and 12.0- $\mu\text{m}$  far-infrared bands has little solar blackbody reflection. It means that the radiation received by the mid-infrared band would be influenced by the reflection of solar radiation reflected by ground surface during the dawn–dusk period (Matson et al., 1987).

Figure 6 gives a schematic diagram of solar blackbody reflection received by satellites.  $z$  is the solar zenith angle, which means the angle between the incident ray of sunlight and the normal to the ground plane. And  $\theta$  is the satellite zenith angle, the angle between the line to the image element of the satellite sensor and the normal to the ground plane. The solar zenith angle determines the illumination conditions during satellite observation. A smaller solar zenith angle has a better illumination condition accompanying with a greater reflected solar radiation received by the satellite. As the scanning



strip of FY-3E is about 2,500 km, it leads to large differences in the solar zenith angle at different detection positions. Therefore, the reflectance of the mid-infrared band needs to be corrected for the solar zenith angle. A typical solar zenith angle correction way is,



$$R' = R / \cos(z) \tag{4}$$

where  $R$  is the original reflectance of the mid-infrared band;  $R'$  is the revised reflectance.

Since FY-3E was observed during the morning and evening hours, the solar zenith angle is very large and  $\cos(z)$  is very small, resulting in a large number of oversaturated pixels when using the correction Eq. 4 (Chen et al., 2022b). Based on the observation experience, the correction equation can be revised to be

$$R' = R / \cos(z \times (1.0 - 1.3 \times \sin(0.05 \times z))) \tag{5}$$



when the solar zenith angle is close to 90°, the correction ratio of Eq. 4 is about 1/8 of that of Eq. 5, which produces far fewer supersaturated image elements. Operational experience has shown that better observation results can be achieved using this method.

### 3.2 Thermal infrared limb-darkening correction

Owing to the effects of the Earth’s curvature and the atmospheric attenuation, the detection data of infrared bands varies depending on the observation angle of the satellite. When the targeted pixel is close to the edge of the satellite’s scanning strip, the radiation reaches the satellite in a very long path, which results in the significant attenuation during the atmospheric propagation.

To eliminate the disparity generated by the satellite’s observation angle, the brightness temperature at the edge of the satellite’s scanning strip needs to be corrected. In this paper, the empirical correction method used in the NESDIS global jigsaw puzzle system is used for correcting the critical dark (Sisong, 1987; Zhong and Yin Hai, 1988). The correction formula is expressed as follows

$$T = T_b + \Delta T \tag{6}$$

$$\Delta T = (e^{0.00012 \times \theta^2} - 1) \times (0.1072 \times T_b - 26.81) \tag{7}$$

where,  $T$  is the revised brightness temperature;  $\Delta T$  is the brightness temperature correction for the satellite zenith angle  $\theta$ ;  $T_b$  is the primary brightness temperature, which is calculated by the Planck law.

$$T_b = C_2 / \ln \left( C_1 \times \frac{\nu^3}{E} + 1 \right) \tag{8}$$

$$\theta = \arcsin \left[ (R_e + H) / R_e \times \sin \varphi \right] \tag{9}$$

where  $C_1$  and  $C_2$  are Planck’s constants;  $E$  is the radiant flux density;  $\nu$  is the central wave number of the band,  $R_e$  is the Earth’s radius;  $\varphi$  is the satellite zenith angle and  $H$  is the instantaneous altitude of the satellite.

### 3.3 Cloud pixels identification

The identification of fire spots is significantly impacted by cloud coverage. On the one hand, clouds can block the radiation information from wildfires on the ground, resulting in missed identification of wildfires. On the other hand, the specular reflection of solar radiation caused by clouds abnormally increases the brightness temperature, which may bring the wildfire misidentification.

As the observation hours of the FY-3E/MERSI-LL is the dawn–dusk period, no other visible light information can be obtained to aid in the identification of cloud pixels (Platnick et al., 2003). Therefore, the Cloud Mask technique, which is widely used for the MODIS cloud identification, cannot be applied into the FY-3E/MERSI-LL (Frey et al., 2008). In this paper, the radiation temperature data which is measured by both

TABLE 3 Criteria for cloud pixel identification.

Number	Criteria
1	$T_{3.8} - T_{10.8} < 4K$
2	$T_{3.8} - T_{10.8} > 20K \ \& \ (T_{3.8} < 275K   T_{10.8} < 270K)$
3	$T_{12.0} < 265K$
4	$T_{10.8} < 270K \ \& \ ((T_{10.8} - T_{12.0}) < 4K   (T_{10.8} - T_{12.0}) > 60K)$

the mid-infrared and far-infrared bands should completely be used to obtain identify the possible cloud pixels. The identification criteria of cloud pixel are presented in Table 3. If any of these criteria is satisfied, the pixel can be identified as a cloud pixel. where,  $T_{3.8}$ ,  $T_{10.8}$ , and  $T_{12.0}$  are the brightness temperature values of mid-infrared 3.8- $\mu\text{m}$ , far-infrared 10.8- $\mu\text{m}$ , and far-infrared 12.0- $\mu\text{m}$  bands, respectively.

### 3.4 Background brightness temperature calculation

The brightness temperature calculation of background is critical for identifying wildfires. It is often derived by using the average brightness temperature of pixels around the targeted pixel. However, background brightness temperature would be influenced by the solar radiation reflection caused by clouds and water, the coverage and types of vegetation, and surrounding fires. These influence factors increase the background brightness temperature, which results in the missed identification of wildfires. Therefore, these suspicious high-temperature pixels should be filtered out before background brightness temperature calculation.

Kaufman et al. (1998) used the standard deviation of background brightness temperature to identify a fire spot, which effectively address the problem of over-calculating the background brightness temperature. The approach used in this study to identify suspicious high-temperature pixels is as follows: Firstly, the top 20% of high-temperature pixels in the monitoring region are chosen as pixels to be recognized. Then, each pixel should be identified successively by using formula (10)

$$T_{3.8} \geq T_{3.8mean} + \min(2 \times T_{3.8std\_bg}, T_{th}) \tag{10}$$

where  $T_{3.8mean}$  and  $T_{3.8std\_bg}$  are the average value and the standard deviation of brightness temperature in the 3.8- $\mu\text{m}$  bands for all pixels in the monitored region, separately;  $T_{th}$  is the background brightness temperature threshold, which is related to the degree of homogeneity of the underlying surface. The initial value of  $T_{th}$  can be set to an initial value of 5 K.

After removing the suspicious high temperature pixels and cloud pixels, the remaining pixels are used to calculate the background brightness temperature information, which includes the average value, as well as the differences of the brightness temperature in the 3.8- $\mu\text{m}$  and the 10.8- $\mu\text{m}$  band. The size of the pixels involved in the calculation of the background brightness temperature is calculated according to

the window method. Firstly, valid  $5 \times 5$  pixels are chosen from the area around the targeted pixel. If the number of valid pixels is less than 20% of the total number of surrounding pixels, the window size of pixels is then expanded to  $7 \times 7$ ,  $9 \times 9$ , and  $11 \times 11$ , gradually. If the condition is still not satisfied when the window size of pixels reaches  $19 \times 19$ , the wildfire identification of this targeted pixel is abandoned.

### 3.5 Wildfire pixel confirmation

The wildfire occurrence of the pixel is confirmed after the calculation of the background brightness temperature. Both absolute and relative threshold criteria are used. The absolute threshold criterion is to compare the brightness temperature of pixels with the predetermined threshold. And the relative threshold criteria are to compare the brightness temperature of the targeted pixel to that of the background pixels in the 3.8- $\mu\text{m}$  band, or to compare the brightness temperature difference between the 3.8- $\mu\text{m}$  and 10.8- $\mu\text{m}$  bands of the targeted pixel to that of the background pixels.

Specifically, if a targeted pixel satisfies the criterion (10) or (11), it can be confirmed as a wildfire pixel. These criteria are more stringent than those of MODIS and FY-3D (Chen et al., 2022a) because of the sizable solar zenith angle non-visible light adjustment throughout the observation period of FY-3E.

$$T_{3.8} > 340K \quad (11)$$

$$\begin{cases} T_{3.8} \geq T_{3.8bg} + a(P_v, P_c, \theta_s) \times \delta T_{3.8bg} \\ T_{3.8-10.8} \geq T_{3.8-10.8bg} + a(P_v, P_c, \theta_s) \times \delta T_{3.8-10.8bg} \\ a(P_v, P_c, \theta_s) = (1.2 \times \sin z_s + 1) \times (1 + P_v) \times (1 + P_c)^2 \end{cases} \quad (12)$$

where  $T_{3.8bg}$  and  $\delta T_{3.8bg}$  are the average and the standard deviation of the brightness temperature in the 3.8- $\mu\text{m}$  bands in the background pixels, separately;  $T_{3.8-10.8}$  is the brightness temperature difference between the 3.8- $\mu\text{m}$  and 10.8- $\mu\text{m}$  bands of the targeted pixel;  $T_{3.8-10.8bg}$  and  $\delta T_{3.8-10.8bg}$  is the value and the standard deviation of the brightness temperature difference between the 3.8- $\mu\text{m}$  and 10.8- $\mu\text{m}$  bands of the background pixels;  $a(P_v, P_c, \theta_s)$  is the correction factor function, which is related to the proportion of non-vegetation pixels  $P_v$ , proportion of cloud pixels  $P_c$ , and solar zenith angle  $z_s$ .

### 3.6 Wildfire extraction from cloud pixels

Traditional fire spot identifications generally skip the procedure of extracting wildfire spots from cloud pixels (Zhong and Yin, 1988; Platnick et al., 2003; Giglio, 2010; Zheng et al., 2020), which may mis-identify parts of wildfires. If the thickness of clouds is thin, a certain amount of radiation energy of wildfire is able to pass through the clouds and reach the satellite, providing a necessary condition for wildfire identification. This study proposes a wildfire identification approach under thin cloud condition with following steps.

#### 1) Potential wildfire selection

A cloud pixel is identified as a potential wildfire pixel when it satisfies the criteria.

$$\begin{cases} T_{3.8} \geq TC_{3.8th} \\ T_{3.8-10.8} \geq T_{3.8-10.8th} \end{cases} \quad (13)$$

where  $TC_{3.8th}$  is the threshold of the brightness temperature in the 3.8- $\mu\text{m}$  band for selecting cloud pixels of potential wildfire;  $T_{3.8-10.8th}$  is the threshold of brightness temperature difference between the 3.8- $\mu\text{m}$  and 10.8- $\mu\text{m}$  bands for selecting cloud pixels of potential wildfire.

#### 2) Wildfire confirmation

The potential wildfire pixel is confirmed as a wildfire pixel if its brightness temperature satisfies the criterion.

$$T_{3.8} \geq T_{3.8bg} + TC_{fireth} \quad (14)$$

where  $TC_{fireth}$  is the cloud pixel fire spot identification threshold.

## 4 Application and comparison

The proposed FY-3E satellite-based wildfire monitoring algorithm has been used in the Shanxi province power grid of State Grid in China since March 2022. It is capable of providing early warning and precise localization of wildfire occurrences. Combined with the coordinate information of transmission lines, it is also able to analyze the danger level of the wildfire to the power system. In this section, two typical wildfire cases were analyzed. And the infrared multispectral data between FY-3E and GMS H8 or GK-2A were compared in the early stage of wildfire occurrences to verify the advantages of FY-3E in the detecting sensitivity as well as the spatial and location accuracy.

### 4.1 Datong wildfire near 220 kV GY transmission line

A wildfire was monitored by FY-3E in Datong City, Shanxi Province, at 16:50 on 30 March 2022. The warning information shows that the location of wildfire was 114.0406°E, 40.4001°N, where is 1.4 km from the 220 kV GY transmission line, and 3 km from five other 220 kV transmission lines, as shown in Figure 7A. Field personnel verified that the actual position of the wildfire was approximately 300 m from the 220 kV GY line, as shown in Figure 7B. Meanwhile, the GMS H8 also detected the wildfire occurrence. However, the warning time of H8 started at approximately 17:00 which was 10 min later than that of FY-3E.

Figure 8 shows a synthesized RGB image of the 3.8, 10.8 and 12- $\mu\text{m}$  infrared bands of FY-3E for the Datong wildfire at 16:50. The red area in the image represents the warning wildfire location which has two pixels, whereas the yellow cross represents the actual location of the wildfire by on-site confirmation. Contrastively, the synthesized RGB images of the 3.8, 0.26, 0.64- $\mu\text{m}$  infrared bands of H8 for the same region at 16:50 and 17:00, separately as shown in Figure 9. It is obvious that the synthesized RGB image of H8 at 16:50 shows

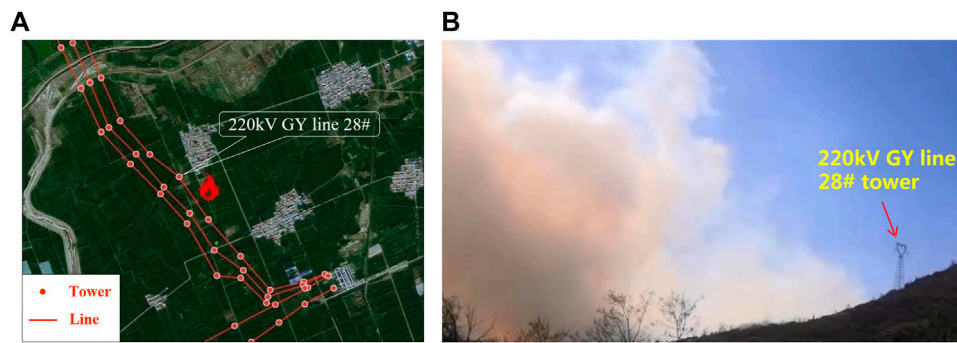


**FIGURE 7**  
(A). Wildfire location and surrounding transmission line; (B). On-site wildfire investigation in Datong city.

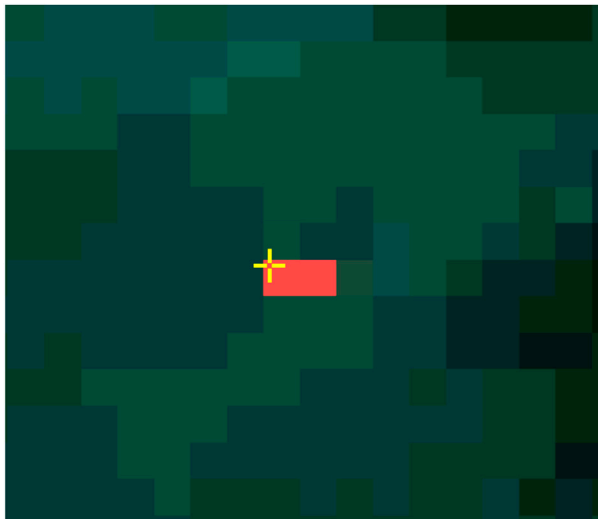


**FIGURE 8**  
RGB composite image of Datong wildfire at 16:50 provided by FY-3E.

little temperature increment at the wildfire location. But at the same time, two temperature abnormal pixels were observed by FY-3E. It was not until 17:00 that GMS H8 observed an unusual brightness temperature at this location with one pixel size.

The brightness temperature of mid-infrared 3.8- $\mu\text{m}$  band for FY-3E and H8 in the wildfire pixels from 16:50 to 17:20 are listed in Figure 10. The brightness temperature of wildfire pixel observed by FY-3E at 16:50 was 322.8 K. It has a difference of 27.1 K from the background brightness temperature, considerably exceeding the identification threshold for the wildfire monitoring. In the contrast, the brightness temperature of pixel observed by H8 was 289.77 K at 16:50, only 0.8 K higher than that of background. The negligible difference of the brightness temperature did not achieve the identification threshold leading to the misidentification of the wildfire at that time. As the wildfire grew intensively, the brightness temperature of H8 increased to 297.92 and

296.11 K at 17:00 and 17:10, respectively. The brightness temperature differences increased to 8.42 and 6.45 K. As a result, H8 issued a wildfire warning at 17:00. But even at this moment, the bright temperature difference between the pixels observed by H8 is much lower than that observed by FY-3E 10 min earlier, indicating FY-3E exhibits a significant higher sensitivity in wildfire detection than H8.

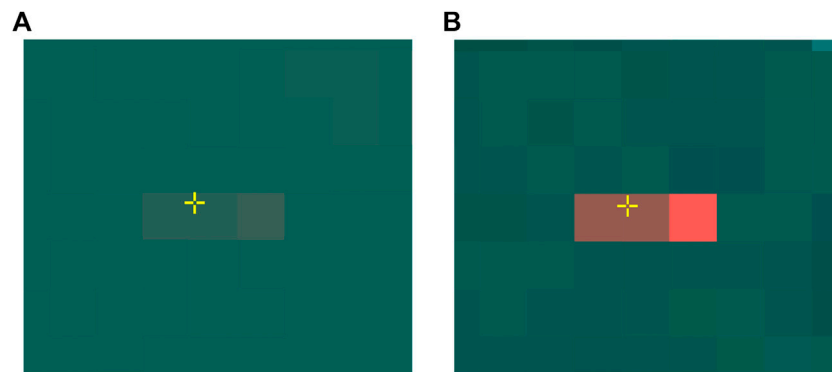
In Figure 8, the two pixels for wildfire monitored by FY-3E covers an area of approximately 2 km<sup>2</sup>. And the satellite-positioned location of the wildfire, which means the geometric center of the pixels, is about 1.12 km away from the actual location of the wildfire (yellow cross). As shown in Figure 9B, GMS H8 monitored a single fire pixel. But the spatial resolution of the pixel is 2 × 2 that covers an area of 4 km<sup>2</sup>. And the distance between the satellite-positioned location and the actual location of the wildfire is approximately 3.25 km, which is as 3 times as that located by FY-3E. Table 4 displays the specific warning information for FY-3E and H8.

## 4.2 Shuozhou wildfire near 500 kV MXI transmission line

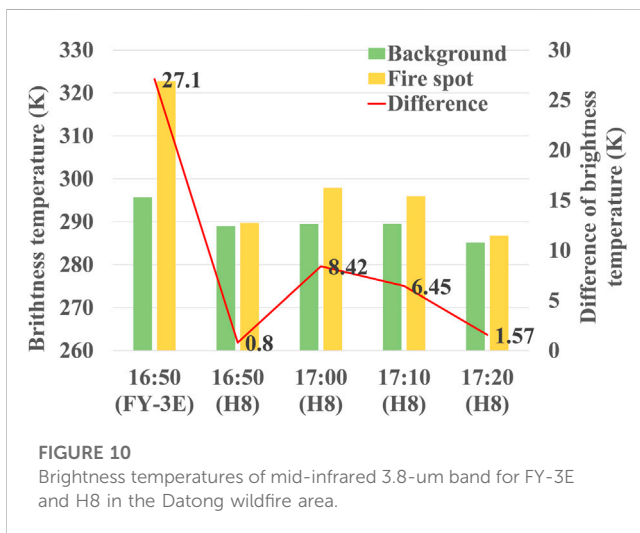
On 7 April 2022, FY-3E detected a wildfire in Shuozhou City, the north of Shanxi Province, at 17:50. As shown in Figure 11, the distance of the warning wildfire zone is less than 500 m from the 500 kV MXI transmission line. Comparatively, GMS GK-2A issue a wildfire warning 18:15, which is 25 min later than FY-3E.

Figure 12 shows the 3.8- $\mu\text{m}$  mid-infrared images when the wildfire was first identified by FY-3E and GK-2A, respectively. Herein, the whiter color indicates the higher brightness temperature of the pixels. And the red boxed area is the final warning pixel of the wildfire. FY-3E has a greater spatial precision than GK-2A. The area of the wildfire identified by FY-3E is 1 km<sup>2</sup>, which is 1/4 of that identified by GK-2A. Moreover, the mid-infrared image of FY-3E contains more detailed brightness temperature information. The brightness temperature of the 3.8- $\mu\text{m}$  mid-infrared channels of FY-3E and GK-2A are compared, as shown in Figure 13. At 17:50, the brightness temperature of wildfire pixel observed by FY-3E was 312.9 K. It has a difference of 8.8 K from the background temperature.





**FIGURE 9** RGB composite images of Datong wildfire provided by H8. (A) 2022-3-30 16:50; (B) 2022-3-30 17:00.



**FIGURE 10** Brightness temperatures of mid-infrared 3.8-um band for FY-3E and H8 in the Datong wildfire area.

However, the brightness temperature of GK-2A was 297.0 K at this time, only 5.6 K than the surrounding background brightness temperature. However, the small brightness temperature increment did not trigger the warning threshold of GK-2A. Until 18:15, the brightness temperature increment increased to 6.1 K, which is higher than the warning threshold of GK-2A. Therefore, GK-2A issued the wildfire warning 25 min later than FY-3E did.

### 5 Conclusion and prospect

Monitoring of wildfire disaster, especially at the extreme weather, is the key to operation governance for electric power

system. Based on the world’s first operational dawn–dusk orbiting PMS FY-3E, this study proposed a wildfire monitoring algorithm to early warn wildfires in transmission line corridors. The following technical contributions can be achieved.

- 1) The proposed algorithm eliminated the adverse effects of large solar zenith angle and differences in satellite viewpoints on the data of infrared band by solar zenith angle correction and thermal infrared limb-darkening correction. And it realized cloud information extraction and wildfire identification from cloud pixels under complex atmospheric conditions, reducing the influence of clouds on false alarms and missed alarms of wildfires.
- 2) Linear spectral separation analysis of the hybrid images shows that the wildfire detection sensitivity of FY-3E is about 4 times higher than that of the H8 and GK-2A, which can significantly improve the detection capability of smaller wildfires in transmission line corridors.
- 3) The proposed FY-3E-based wildfire monitoring algorithm has been applied in China’s Shanxi Power Grid. The application experience demonstrates that the FY-3E-based algorithm has obvious advantages in terms of the detecting sensitivity, as well as the spatial and localization accuracy, compared to that of GMSs H8 and GK-2A. The wildfire positioning accuracy of FY-3E can be improved by more than one times.

It should be noted that, although FY-3E has higher sensitivity and localization accuracy in detecting wildfires, it has a very low frequency of monitoring, bringing the monitoring limitations in wildfires with short duration and rapid changes. And FY-3E is also unable to monitor the development of wildfire continuously

**TABLE 4** Datong wildfire warning information of FY-3E and H8.

Satellite	Warning time	Wildfire pixel number	Monitored wildfire area (km <sup>2</sup> )	East-west length of wildfire pixels (km)	South-north length of wildfire pixels (km)	Locating deviation of wildfire (km)
FY-3E	16:50	2	1.9	1.7	1.1	1.12
H8	17:00	1	3.9	1.7	2.3	3.25

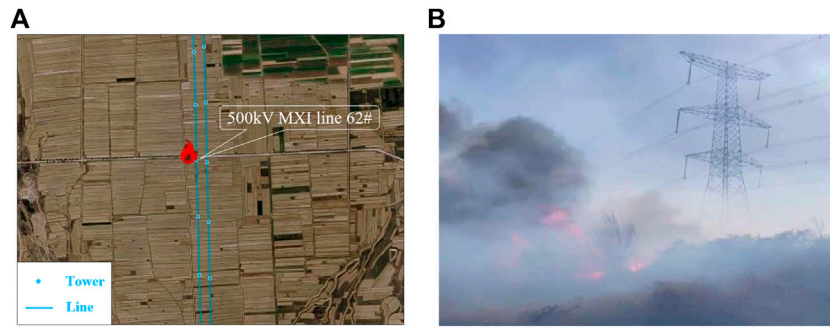


**FIGURE 11**  
(A). Wildfire location and surrounding transmission line; (B). On-site wildfire investigation in Shuozhou city.

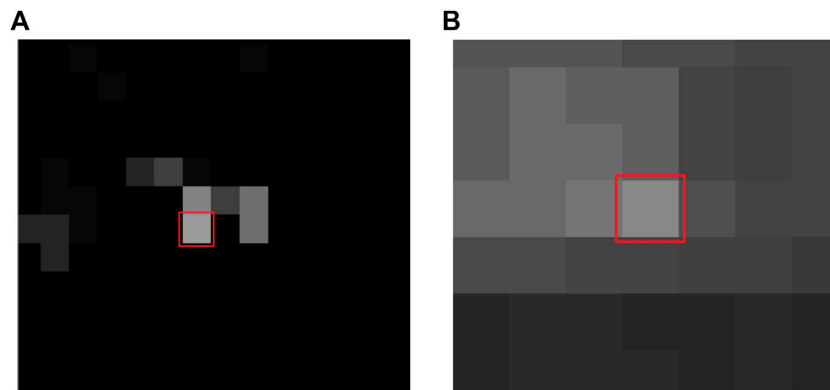


**FIGURE 12**  
3.8- $\mu\text{m}$  mid-infrared image of Shuozhou wildfire provided by (A) FY-3E at 2022-4-7 17:50 and (B) GK-2A at 2022-4-7 18:15.

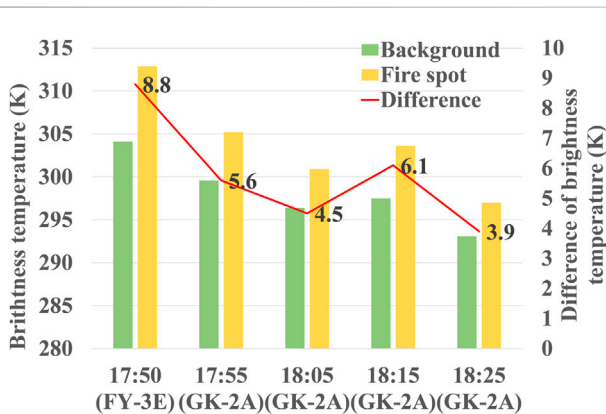


**FIGURE 13**  
Brightness temperatures of mid-infrared 3.8- $\mu\text{m}$  band for FY-3E and H8 in the Shuozhou wildfire area.

enhance the effect of satellite remote sensing wildfire monitoring. On the other hand, although this paper proposes a method for wildfire identification under thin cloud conditions, cloud cover is still the main reason for the missed monitoring of wildfires. Therefore, how to effectively combine satellite monitoring with multiple technical methods such as helicopters, drones, manual patrols and fixed monitoring devices to realize complementary advantages is the future direction to enhance the monitoring and warning capability of wildfires on power grid transmission lines.

### Data availability statement

The raw data supporting the conclusion of this article will be made available by the authors, without undue reservation.

### Author contributions

JL: Conceptualization, Methodology, Writing-original draft, Formal Analysis. JC: Writing-original draft, Project

and dynamically. In order to meet the requirements of high accuracy and timeliness of wildfire monitoring in transmission corridors, the subsequent study will combine the use of FY-3E and GK-2A, H8 through data fusion technologies to further

administration, Resources. HY: Writing–review and editing, Methodology. MJ: Writing–review and editing, Validation. ZL: Writing–review and editing, Supervision. YZ: Writing–review and editing, Data curation, Methodology. SW: Validation, Writing–review and editing. JF: Supervision, Writing–review and editing.

## Funding

The author(s) declare financial support was received for the research, authorship, and/or publication of this article. The research was funded by the Science and technology projects funded by National Key Research and Development Program of China for supporting this research under Contract No. 2021YFC3000300, and by State Grid Shanxi Electric Power Company Technology Project under Contract No. 52053023000D.

## References

- Anagnostatos, S. D., Halevidis, C. D., Polykrati, A. D., Koufakis, E. I., and Bourkas, P. D. (2011). High-Voltage lines in fire environment. *IEEE Trans. Power Deliv.* 26 (3), 2053–2054. doi:10.1109/TPWRD.2011.2123471
- Blackett, M. (2015). An initial comparison of the thermal anomaly detection products of MODIS and VIIRS in their observation of Indonesian volcanic activity. *Remote Sens. Environ.* 171, 75–82. doi:10.1016/j.rse.2015.10.002
- Chen, J., Yao, Q., Chen, Z., Li, M., Hao, Z., Liu, C., et al. (2022a). The fengyun-3D (FY-3D) global active fire product: principle, methodology and validation. *Earth Syst. Sci. Data.* 14 (8), 3489–3508. doi:10.5194/essd-14-3489-2022
- Chen, J., Zheng, W., Wu, S., Liu, C., and Yan, H. (2022b). Fire monitoring algorithm and its application on the geo-kompsat-2A geostationary meteorological satellite. *Remote Sens.* 14 (11), 2655. doi:10.3390/rs14112655
- Chen, W., Zhou, Y., Chen, J., Zhou, E., Zhou, W., and Sui, S. (2019). “Wildfire monitoring technology of transmission lines based on himawari-8 geostationary meteorological satellite,” in 2019 IEEE 3rd Conference on Energy Internet and Energy System Integration (EI2), Changsha, China, 08–10 November 2019, 2408–2412. doi:10.1109/EI247390.2019.9061748
- Dong, C., Weng, F., and Yang, J. (2022). Assessments of cloud liquid water and total precipitable water derived from FY-3E MWTS-III and NOAA-20 ATMS. *Remote Sens.* 14 (8), 1853. doi:10.3390/rs14081853
- Dozier, J. (1981). A method for satellite identification of surface temperature fields of subpixel resolution. *Remote Sens. Environ.* 11, 221–229. doi:10.1016/0034-4257(81)90021-3
- El-Zohri, E. H., Abdel-Salam, M., Shafey, H. M., and Ahmed, A. (2013). Mathematical modeling of flashover mechanism due to deposition of fire-produced soot particles on suspension insulators of a HVTL. *Electr. Power Syst. Res.* 95, 232–246. doi:10.1016/j.epsr.2012.09.009
- Fan, X., Pang, X., and Feng, H. (2022). Design of multi-data sources based forest fire monitoring and early warning system. *Big Data – BigData 2022*, 35–51. doi:10.1007/978-3-031-23501-6\_5
- Fonseca, J. R., Tan, A. L., Silva, R. P., Monassi, V., Assuncao, L. A. R., Junqueira, W. S., et al. (1990). Effects of agricultural fires on the performance of overhead transmission lines. *IEEE Trans. Power Deliv.* 5 (2), 687–694. doi:10.1109/61.53071
- Frey, R. A., Ackerman, S. A., Liu, Y., Strabala, K. I., Zhang, H., Key, J. R., et al. (2008). Cloud detection with MODIS. Part I: improvements in the MODIS cloud Mask for collection 5. *J. Atmos. Ocean. Technol.* 25 (7), 1057–1072. doi:10.1175/2008JTECHA1052.1
- Frost, P., and Annegarn, H. (2007). “Providing satellite-based early warnings of fires to reduce fire flashovers on South Africa’s transmission lines,” in 2007 IEEE International Geoscience and Remote Sensing Symposium, Barcelona, Spain, 23–28 July 2007, 2443–2446. doi:10.1109/IGARSS.2007.4423336
- Giglio, L. (2010). *MODIS collection 5 active fire product user’s guide version 2.4, science systems and applications*. Maryland: University of Maryland.
- Hillger, D., Kopp, T., Lee, T., Lindsey, D., Seaman, C., Miller, S., et al. (2013). First-light imagery from suomi NPP VIIRS. *Bull. Am. Meteorological Soc.* 94 (7), 1019–1029. doi:10.1175/BAMS-D-12-00097.1

## Conflict of interest

The authors declare that this study received funding from State Grid Shanxi Electric Power Company The funder had the following involvement in the study: collection and interpretation of data.

The authors declare that the research was conducted in the absence of any commercial or financial relationships that could be construed as a potential conflict of interest.

## Publisher’s note

All claims expressed in this article are solely those of the authors and do not necessarily represent those of their affiliated organizations, or those of the publisher, the editors and the reviewers. Any product that may be evaluated in this article, or claim that may be made by its manufacturer, is not guaranteed or endorsed by the publisher.

- Kaufman, Y. J., Kleidman, R. G., and King, M. D. (1998). SCAR-B fires in the tropics: properties and remote sensing from EOS-MODIS. *J. Geophys. Res. Atmos.* 103 (D24), 31955–31968. doi:10.1029/98JD02460
- Liang, Y., Zhou, L., Chen, J., Huang, Y., Wei, R., and Zhou, E. (2020). Monitoring and risk assessment of wildfires in the corridors of high-voltage transmission lines. *IEEE Access* 8, 170057–170069. doi:10.1109/ACCESS.2020.3023024
- Lu, J., Liu, Y., Zhang, G., Li, B., He, L., and Luo, J. (2018). Partition dynamic threshold monitoring technology of wildfires near overhead transmission lines by satellite. *Nat. Hazards* 94 (3), 1327–1340. doi:10.1007/s11069-018-3479-5
- Martin, M. P., Ceccato, P., Flasse, S., and Downey, I. (1999). *Fire detection and fire growth monitoring using satellite data*. Berlin, Heidelberg: Springer Berlin Heidelberg.
- Matson, M., Stephens, G., and Robinson, J. (1987). Fire detection using data from the NOAA-N satellites. *Int. J. Remote Sens.* 8 (7), 961–970. doi:10.1080/0143168708954740
- Platnick, S., King, M. D., Ackerman, S. A., Menzel, W. P., Baum, B. A., Riedi, J. C., et al. (2003). The MODIS cloud products: algorithms and examples from terra. *IEEE Trans. Geoscience Remote Sens.* 41 (2), 459–473. doi:10.1109/TGRS.2002.808301
- Roy, D. P., Boschetti, L., and Smith, A. M. S. (2013). “Satellite remote sensing of fires,” in *Fire phenomena and the earth system: An interdisciplinary guide to fire science*. Editor C. M. Belcher (John Wiley & Sons), 77–93.
- Shan, T., Zheng, W., Chen, J., and Tang, S. (2021). A burned area mapping method for the FY-3D MERSI based on the single-temporal L1 data and multi-temporal daily active fire products. *Int. J. Remote Sens.* 42 (4), 1292–1310. doi:10.1080/01431161.2020.1826064
- Shengli, W., and Cheng, L. (2010). “A new model for fire forecast,” in *Proc. SPIE 7831, earth resources and environmental remote sensing/GIS applications*. Editors U. Michel and D. L. Civco (SPIE), 184–189. doi:10.1117/12.865533
- Sisong, Z. (1987). The application of avhrr data to estimating the earth-atmosphere radiation budget of the qinghai-xizang plateau. *Atmos. Radiat.*, 139–144. doi:10.1007/978-1-935704-18-8\_23
- Su, H., Sun, M., and Shang, J. (2019). “Research on stereoscopic monitoring and positioning technology of mountain fire in EHV transmission lines,” in 2019 IEEE 3rd International Electrical and Energy Conference (CIEEC), Beijing, China, 07–09 September 2019, 222–227. doi:10.1109/CIEEC47146.2019.CIEEC-2019115
- Wang, C.-H. (2022). *Bushfire and climate change risks to electricity transmission networks*. Cham: Springer International Publishing.
- Wang, Y., Chen, C., Wang, J., and Baldick, R. (2016). Research on resilience of power systems under natural disasters—a review. *IEEE Trans. Power Syst.* 31 (2), 1604–1613. doi:10.1109/TPWRS.2015.2429656
- Wooster, M. J., Roberts, G. J., Giglio, L., Roy, D. P., Freeborn, P. H., Boschetti, L., et al. (2021). Satellite remote sensing of active fires: history and current status, applications and future requirements. *Remote Sens. Environ.* 267, 112694. doi:10.1016/j.rse.2021.112694

- Xie, L., Wu, S., Chen, J., Zheng, W., Yan, H., and Xu, Z. (2022). Cross-Comparison of channel parameters between FY-3E/MERSI-LL and Himawari-8/AHI in China. *Int. J. Remote Sens.* 43 (12), 4663–4681. doi:10.1080/01431161.2022.2116297
- You, F., Zhang, Y., Chen, H.-x., Zhang, L.-h., Zhu, J.-p., and Zhou, J.-j. (2013). Preliminary studies on flashovers of high-voltage transmission lines induced by wildfires by field survey and experimental tests. *Procedia Eng.* 52, 557–565. doi:10.1016/j.proeng.2013.02.185
- Yu, F., and Wu, X. (2016). Radiometric inter-calibration between himawari-8 AHI and S-NPP VIIRS for the solar reflective bands. *Remote Sens.* 8 (3), 165. doi:10.3390/rs8030165
- Zhang, P., Hu, X., Lu, Q., Zhu, A., Lin, M., Sun, L., et al. (2022). FY-3E: the first operational meteorological satellite mission in an early morning orbit. *Adv. Atmos. Sci.* 39 (1), 1–8. doi:10.1007/s00376-021-1304-7
- Zhang, W., Yu, H., Yan, Z., and Xu, J. (2017). “Study on disaster monitoring technology of mountain fire based on UAV transmission line inspection,” in 2017 IEEE International Conference on Unmanned Systems (ICUS), Beijing, China, 27–29 October 2017, 400–403. doi:10.1109/ICUS.2017.8278377
- Zheng, W., Chen, J., Yan, H., Liu, C., and Tang, S. (2020). Global fire monitoring products of FY-3D/MERSI-II and their applications. *J. Remote Sens.* 24 (5), 521–530. doi:10.11834/jrs.20209177
- Zhong, Q., and Yin Hai, L. (1988). Satellite observation of surface albedo over the qinghai-xizang plateau region. *Adv. Atmos. Sci.* 5 (1), 57–65. doi:10.1007/BF02657346
- Zhou, F., Ma, Y., and Wang, H. (2020). “Research on transmission line fire monitoring technology based on remote sensing satellite data,” in 2020 International Conference on Urban Engineering and Management Science (ICUEMS), Zhuhai, China, 24–26 April 2020, 314–317. doi:10.1109/ICUEMS50872.2020.00075